

Research Article

Hybridization State Detection of DNA-Functionalized Gold Nanoparticles Using Hyperspectral Imaging

Richard C. Murdock,^{1,2} Omar A. Khan,² Thomas J. Lamkin,² Saber M. Hussain,² and Nancy Kelley-Loughnane¹

¹*Airman Systems Directorate, 711th Human Performance Wing, Wright-Patterson AFB, Human Signatures Branch (711 HPW/RHXB), Dayton, OH, USA*

²*Airman Systems Directorate, 711th Human Performance Wing, Wright-Patterson AFB, Molecular Bioeffects Branch (711 HPW/RHDJ), Dayton, OH, USA*

Correspondence should be addressed to Nancy Kelley-Loughnane; nancy.kelley-loughnane.1@us.af.mil

Received 6 July 2016; Accepted 13 October 2016; Published 21 March 2017

Academic Editor: Marek Samoc

Copyright © 2017 Richard C. Murdock et al. This is an open access article distributed under the Creative Commons Attribution License, which permits unrestricted use, distribution, and reproduction in any medium, provided the original work is properly cited.

Hyperspectral imaging has the unique ability of capturing spectral data for multiple wavelengths at each pixel in an image. This gives the ability to distinguish, with certainty, different nanomaterials and/or distinguish nanomaterials from biological materials. In this study, 4 nm and 13 nm gold nanoparticles (Au NPs) were synthesized, functionalized with complimentary oligonucleotides, and hybridized to form large networks of NPs. Scattering spectra were collected from each sample (unfunctionalized, functionalized, and hybridized) and evaluated. The spectra showed unique peaks for each size of Au NP sample and also exhibited narrowing and intensifying of the spectra as the NPs were functionalized and then subsequently hybridized. These spectra are different from normal aggregation effects where the LSPR and reflected spectrum broaden and are red-shifted. Rather, this appears to be dependent on the ability to control the interparticle distance through oligonucleotide length, which is also investigated through the incorporation of a poly-A spacer. Also, hybridized Au NPs were exposed to cells with no adverse effects and retained their unique spectral signatures. With the ability to distinguish between hybridization states at nearly individual NP levels, this could provide a new method of tracking the intracellular actions of nanomaterials as well as extracellular biosensing applications.

1. Introduction

Gold nanoparticles (Au NPs) have been highly popular for use in cell imaging, targeted drug delivery, cancer diagnostics, and medical therapeutic applications [1–4]. In general, Au NPs serve as a model system for NP studies due to their large, producible size and shape ranges and their ease of functionalization with biomolecules through thiol chemistry. Traditionally, these NPs have been considered nontoxic [5, 6]; however, studies have shown that Au NPs can display toxicity based on factors such as size, charge, and surface modifications [7–10]. The growing interest in Au and other noble metal NPs is due to their intense local surface plasmon resonance (LSPR). Au NP's LSPRs are sensitive to the NP's surrounding environment, causing a significant shift in the

LSPR peak when in close proximity to other materials or when molecules interact with their surface. This shift in the LSPR peak can be measured by observing the changes in the absorption spectrum; however, it also correlates to a change in the scattered light from the particle, providing a colorimetric response which is recordable by any light scattering spectrum equipment. Each technique, whether it is absorption or scattering, provides an easy mechanism by which the local environment of the NPs can be determined with high sensitivity. Using the LSPR measurement of the NPs makes these materials ideal for sensor type applications since additional tagging, such as fluorescence labeling of the NPs, is not needed for tracking or identifying the NP state [5, 6]. Chemical sensing using functionalized Au or Ag nanospheres and nanorods has been successful in detecting DNA, heavy

metal ions, and immunoproteins, among other targets, at concentrations into the single nanomolar regime as well as solution pH changes [7, 11–16]. Many of these sensor applications use biomolecules, specifically oligonucleotides, to perform targeted biomolecule capture and provide a concentration dependent, colorimetric response to the binding event [17–19]. Also, core-satellite assembly of Au and Ag NPs via oligonucleotides showed potential enhancement of LSPR effects [20, 21]. Recently, ordered crystalline networks of DNA hybridized particles have shown the potential for nanometer-specific arrangement of Au NPs of different shapes, leading to unique, and potentially tunable, spectral signatures of these networks [22]. The ability to optically tune these Au NP networks can lend itself to producing targeted delivery or sensing mechanisms.

Imaging spectroscopy has been used for many years in the realm of earth sciences, specifically for studying Earth's surface features, weather, and even the chemical makeup of stars [23]. Hyperspectral imaging obtains an image where each pixel in the image contains the complete spectral signature of a material by using many contiguous channels that sample very narrow portions of the electromagnetic spectrum. Even though significant technical differences in data collection methods exist between spectral microscopy and hyperspectral remote sensing, the output data is nearly identical. Therefore, many of the analysis methods developed for earth imaging applications can be directly applied to spectral microscopy. In this study, hyperspectral imaging is used in conjunction with microscopy techniques to examine the unique scattering spectra of functionalized and hybridized Au NPs for potential intracellular indicators of binding events.

2. Materials and Methods

2.1. Synthesis of Gold Nanoparticles. The synthesis of gold colloids in the size range of 10–15 nm has been performed in numerous publications. The method described here is an adaptation of the methods cited [24–28]. 500 mL of 0.04% w/v (~0.001 M) gold (III) chloride trihydrate (MP Biomedicals, Solon) was heated to a rapid boil under vigorous stirring. Next, 50 mL of 1.14% w/v (~0.0388 M) trisodium citrate dihydrate (Fluka, St Louis) was added rapidly to the vortexing solution. The solution was held at boiling and was stirred for an additional 10 min. The flask was then moved to a nonheated stir plate to continue stirring while the solution was cooled to room temperature. The suspension was filtered through a 0.22 μm filter into a brown glass container for storage at room temperature.

To synthesize the 4 nm Au colloid, stock solutions of 0.4% w/v (~0.01 M) gold (III) chloride trihydrate, 1.0% w/v (~0.034 M) trisodium citrate dihydrate, and 0.5% w/v (~0.132 M) sodium borohydride (Sigma-Aldrich, St Louis) were all freshly prepared. The following synthesis process was adapted from literature methods [29–32]. To begin synthesis, 50 mL of deionized (DI) H₂O (Millipore, resistivity (ρ) = 18.2 M Ω cm) was transferred into a 100 mL glass beaker with a small magnetic stir bar in the bottom. Next, 1.25 mL of 0.4% HAuCl₄ was added to the solution in the beaker

and all solutions were kept at 4°C. The beaker was then placed on a magnetic stir plate where the solution was mixed vigorously for approximately 1 min. Next, 500 μL of 0.5% NaBH₄ was added rapidly to the solution while continuing to stir vigorously for 1 min. After 1 min, 200 μL of 1.0% Na₃C₆H₅O₇ was added to the solution and continued to stir for an additional 1 min. Finally, the solution was filtered through a 0.22 μm syringe filter into a brown glass container and stored at 4°C.

2.2. Nanomaterial Characterization

2.2.1. Transmission Electron Microscopy (TEM). TEM characterization was performed to obtain the primary particle size and morphology of NPs using a Hitachi H-7600 tungsten-tip instrument at an accelerating voltage of 100 kV in high resolution mode. NPs were examined after deposition of 5 μL of each stock sample onto 200 mesh formvar/carbon-coated copper TEM grids which were then allowed to air-dry. In addition to observing general morphology of the NPs, the mean particle size and standard deviation for each sample were calculated from measuring over 100 NPs in random fields of view using ImageJ software [33].

2.2.2. Dynamic Light Scattering (DLS) and Laser Doppler Velocimetry (LDV). DLS and LDV were used to verify size and surface charge changes of the NPs after functionalization or hybridization were performed on a Malvern Instruments Zetasizer Nano-ZS instrument. Samples were examined after dilution of NP stock solutions in DI water, vortexed to provide a homogeneous solution, and then 1 mL was transferred to a Malvern Clear Capillary cell for DLS and LDV measurements [33].

2.2.3. UV-Visible Absorption Spectroscopy (UV-Vis). The absorption spectra of the NMs were collected on the Cary UV-Vis 300 Spectrophotometer with WinUV software (Varian, Inc.). Samples were measured at full stock concentration, half stock concentration, or one-tenth of stock concentration, depending on original concentration, and diluted using either DI H₂O or hybridization buffer (NaCl). For dehybridization scans, the solutions were also placed in a quartz cuvette and the instrument was set to measure OD at 280 nm while the temperature was increased at steps of 2°C every 2 min recording any change in the absorption. Molar particle concentrations were calculated using the Beer-Lambert Law, $A = \epsilon lc$, and extinction coefficient values for Au NPs were obtained from literature sources [21, 34].

2.3. Functionalization of Gold Colloids. Two complementary sets of oligonucleotides were obtained from Integrated DNA Technologies, Inc. Sequence A1 (5'-HS-AAAAA-AAAACGCATTCAGCATTCT-3') and sequence C1 (5'-HS-AAAAAAAAAAGAATCCTGAATGCG-3') are complementary and both contain a poly-A spacer. Sequence A1-pA (5'-HS-CGCATTCAGCATTCT-3') and sequence C1-pA (5'-HS-AGAATCCTGAATGCG-3') are complementary and are lacking the poly-A spacer. All sequences contain a thiol modification (HS-) at the 5' end of the sequence.

The functionalization methods used for both Au NPs were adapted from similar literature procedures [17, 19–21, 28, 35].

To standardize the functionalization procedure for the following colloidal materials, the 13 nm Au colloids were chosen to begin with since they are easily functionalized and do not require any special centrifugation. First, 3 mL of the 13 nm Au NPs from stock concentration of ~13 nM was placed into scintillation vials separately for each DNA sequence. Next, 20 μL of each 1 mM DNA sequence was added to the different scintillation vials while stirring briefly. The mixture was then let to sit in the dark for 20 min without stirring. Following this, 366 μL of 100 mM potassium phosphate buffer (PB) (Sigma) was added to each mixture, and a total of 275 μL of 2 M NaCl (Sigma) solution was added to each Au-DNA mixture over 20 min. The Au-DNA mixture was left at room temperature overnight in the dark. The Au-DNA mixtures were then centrifuged at 16,000 $\times g$ for 14 min. The supernatant was removed and each pellet was resuspended in 100 μL of 100 mM NaCl and 25 mM Tris Acetate (pH 8.2) solution. This washing process was repeated twice more with centrifugation at 16,000 $\times g$ for 12 min. After the final washing, the pellets were resuspended in hybridization buffers of different NaCl concentrations dependent upon the melting temperature, or dehybridization temperature, desired. For the 13 nm Au-DNA NPs, this was either 100 μL of 50 mM NaCl and 25 mM Tris Acetate (pH 8.2) or 100 μL of 100 mM NaCl and 25 mM Tris Acetate (pH 8.2) solutions. A sample of each Au-DNA mixture was measured by UV-Vis spectroscopy to determine the concentration of each solution. Using this information, equimolar amounts of each complementary Au-DNA samples were combined in a new microcentrifuge tube and stored at 4°C overnight for hybridization. The following day, the samples were vortexed to resuspend any settled aggregates of NPs prior to use.

To functionalize the 4 nm Au NPs, 3 mL of ~130 nM NPs was placed into scintillation vials separately for each DNA sequence. The procedure is similar to the functionalization procedure for the 13 nm Au NPs, with the following adaptations due to the small size of the particles. The 4 nm Au-DNA mixtures were aliquoted into ultracentrifuge tubes and centrifuged at 261,600 $\times g$. For the hybridization buffer, either 200 μL of 300 mM NaCl and 25 mM Tris Acetate (pH 8.2) or 200 μL of 500 mM NaCl and 25 mM Tris Acetate (pH 8.2) solutions were added to the samples.

2.4. Cell Culture. Immortalized human keratinocytes (HaCaT cells) were used as a cellular model to determine the interaction of NPs with human skin. HaCaT cells were donated generously by Dr. James F. Dillman III, of the US Army Medical Research Institute of Chemical Defense. The culture media for the HaCaT cells consisted of RPMI-1640 (ATCC) supplemented with 10% fetal bovine serum (ATCC) and 1% penicillin-streptomycin (Sigma). The cells are grown in 75 cm² vented flasks in a humidified incubator at a temperature of 37.0°C and 5% CO₂ [36]. The cells were passaged using 0.25% trypsin with EDTA (GIBCO) when they reached 80% confluence and reseeded using a dilution ratio of 1:10.

2.5. Biocompatibility Assessment

2.5.1. Cell Viability. Dosing solutions of the unfunctionalized, functionalized, and hybridized 13 nm Au NPs were made in the HaCaT cell culture media at a molar particle concentration of 2.5 nM, as determined by UV-Vis spectroscopy. Cell viability was assayed using the CellTiter 96® Aqueous One Solution Cell Proliferation Assay (Promega). This assay is a colorimetric method used to determine the number of viable cells in proliferation or cytotoxicity experiments. HaCaT cells were seeded at 30,000 cells/cm² and the PC-12 cells were seeded at 40,000 cells/cm² in a 96-well, flat-bottom culture plate with 200 μL per well. The cells were grown for 24 h in a humidified, 5% CO₂ incubator at 37°C until ~80% confluent. Existing media were aspirated and 200 μL of the dosing solutions was added to the wells. The cultures were incubated for an additional 24 h, at which point the dosing solutions were aspirated, and the cells were washed three times with 100 μL of 1x phosphate buffered saline solution (PBS). Next, 100 μL of complete culture media and 20 μL of the CellTiter 96® Aqueous One reagent were added to each well and then incubated for 1 h at 37°C. The plates were then placed on a plate stirrer for a few minutes to evenly distribute the MTS product in each solution for consistent measurements. Plates were measured using a BioTek Synergy HT spectrophotometer with GenX 5 software for sample absorbance at a wavelength of 490 nm. The relative cell viability (%) of the NP dosed wells was compared to control wells. Each experiment was performed in triplicate, and the data are represented as the mean \pm standard deviation with $n \geq 25$ for each sample. Statistics were run on the data using a one-way ANOVA test in JMP 7.0.

2.5.2. Nanomaterial Uptake. To evaluate the uptake of the NPs into the cells, treated cells were sectioned and imaged under TEM. A modified procedure of the method published by Schrand et al. (2010) was used [37]. HaCaT cells were seeded at 30,000 cells/cm² (2 mL volume/well) into a flat-bottom, 6-well cell culture plate and incubated at 37°C for 24 h. The media were aspirated from each well, and 2 mL of 2.5 nM dosing solutions of 4 nm Au NPs in complete media was added to 4 wells. Media without NPs were added to 2 wells (control samples). After a 24 h exposure, the media were aspirated, and 1 mL of 0.25% trypsin with EDTA was added to each well and incubated at 37°C for 5 min to detach the cells from the bottom of the plate. Each cell solution was then transferred to a 15 mL conical tube and 5 mL of complete media was added to each sample. The cells were centrifuged for 10 min at 800 $\times g$. The supernatant was removed, and the cell pellets were transferred to conical-tipped embedding capsules (BEEM, EMS). Next, 500 μL of 2% paraformaldehyde (diluted with PBS) was added to each pellet and fixed overnight at 4°C. The paraformaldehyde solution was removed, and the pellet was rinsed 3 times for 30 min each with 1x PBS. Cell pellets were stained using 300 μL of 1% osmium tetroxide (OsO₄) (EMS), which was diluted in PBS, for 1 h. OsO₄ was removed from each pellet and neutralized in corn oil. Cell pellets were rinsed with PBS 3 times for 10 min each to remove remaining OsO₄. Next, the pellets

were dehydrated using decreasing ethanol (EtOH) dilutions prepared in water. First, 300 μL of 50% EtOH was added to each pellet for 10 min. The solution was removed and 300 μL of 70% EtOH was added 3 times for 10 min each, removing the solution each time. Next, 300 μL of 80% EtOH was added to each pellet for 10 min, followed by removal of the solution and addition of 300 μL of 90% EtOH 10 min. The previous solution was removed, and 300 μL of 100% EtOH was added 3 times for 10 min each, with removal of the solution after each time period. Finally, 300 μL of a 1:1 dilution of 100% EtOH and LR White resin (EMS) was added to each sample for 1 h. The embedding capsule was then filled the rest of the way with resin, and the samples were placed in a vacuum oven overnight at 60°C to cure. Ultramicrotome sectioning of the samples was performed according to the procedure described by Schrand et al. (2010) on a Leica EM UC7 ultramicrotome using an Ultra 45° diamond knife (DiATOM). Sections were placed on 200-mesh, formvar/carbon-coated copper grids and imaged using a Hitachi H-7600 tungsten-tip instrument at an accelerating voltage of 100 kV in high contrast mode.

2.6. Hyperspectral Imaging. Hyperspectral imaging (HSI) was performed on the CytoViva Hyperspectral Imaging System (HSI) (CytoViva, Inc., Auburn). This system is capable of capturing spectral information from 400 nm to 1,000 nm in wavelength with 1.29 nm spectral resolution. The light source is a 150 W halogen light source connected to the CytoViva high resolution illuminator which is a highly collimated darkfield condenser, similar to systems used in previous NP-SPR darkfield studies [38, 39]. NP samples were prepared by spotting 10 μL of the stock solution onto a glass microscope slide, applying a cover glass, and sealing the cover glass with clear epoxy around the edges. The slide was then let to sit for 30 min to 1 h to allow the NPs to settle prior to being scanned.

For imaging of NPs with cells, HaCaT cells were plated in dual chambered slides at a cell density of 30,000 cells/cm² and incubated for 24 h. The media was aspirated and the cells were dosed with 13 nm Au A1-pA + C1-pA at a concentration of 2.5 nM in complete media for an additional 24 h. The control cells were not dosed but did undergo a media change at the same timepoint as the treated cells. The media was removed and the cells were fixed in 1 mL of 4% paraformaldehyde in PBS for 10 min at room temperature. The cells were then rinsed 3 times with PBS, and then the chambers were removed from the slides. A 10 μL drop of PBS was added to each sample square and then a cover slip was placed over each sample and sealed with clear nail polish.

Spectra were obtained from NP only samples by selecting individual pixels multiple times in areas of interest within the image to build a spectral library. For the samples containing cells and NPs, spectra were obtained from pixels in areas where NPs appeared to be interacting with the cells. Due to differences in sample scattering, exposure times must be optimized for each sample imaged; therefore, it is not possible to compare intensity values of spectra obtained from different samples. All scan information was collected and processed through ENVI software.

3. Results

3.1. Transmission Electron Microscopy and Visual Solution Images. Primary particle mean size of the 13 nm Au NPs was 12.6 ± 0.96 nm and of the 4 nm Au NPs was 3.88 ± 1.14 nm (Figure S1). All samples exhibited consistent spherical morphology (Figure S1 in Supplementary Material available online at <https://doi.org/10.1155/2017/8427459>). TEM was used to visualize the hybridized NPs, in this case the 13 nm Au A1 + C1 NPs, which demonstrates the large 3-dimensional networks of NPs that are formed when the DNA hybridizes (Figures 1(a) and 1(b)). Functionalization of the 13 nm Au NPs with different oligonucleotide sequences did not alter the particle morphology (Figure 1(b)). Also, fairly uniform spacing of the 13 nm Au NPs is observed (Figure 1(b)). The 4 nm Au A1 + C1 NPs are shown in Figure 1(c), forming networks 200 to 300 nm in size with the high salt concentration necessary to hybridize these NPs evident in the image. The 4 nm Au A1-pA + C1-pA NPs formed large, tightly packed networks microns in size (Figure 1(d)) with salt residue visible under TEM for this sample also. The difference in the oligonucleotide lengths, due to the presence of the poly-A sequence, can be observed when comparing the interparticle spacing of the 4 nm Au A1 + C1 NPs to that of the 4 nm Au A1-pA + C1-pA NPs (Figures 1(c) and 1(d)).

3.2. UV-Vis Spectroscopy. The UV-Vis spectra obtained for the 13 nm Au NPs are shown in Figure S2. The absorption maxima for the 13 nm Au NPs occurred at a wavelength of 520 nm, which correlates well to literature values [32]. Using an extinction coefficient of $1.39E8 \text{ M}^{-1} \text{ cm}^{-1}$ [32], the molar particle concentration was determined to be ~ 10 nM. The absorption maximum for the 4 nm Au NPs was measured at 506 nm (Figure S2D) and the molar particle concentration was determined to be ~ 167 nM. The values for the 4 nm Au NPs compare well to theoretical values and also demonstrate the blue-shift of the LSPR peak as particle size decreases when compared to the 13 nm Au NP spectra. The A_{SPR}/A_{450} ratio is also in good agreement with literature values at 1.18 compared to a value of 1.19, which was theoretically determined [34, 40].

All individually functionalized 13 nm and 4 nm Au NPs demonstrated the red appearance of the original solutions prior to functionalization (Figures S2A and S2C). However, the hybridized 13 nm samples (A1 + C1 and A1-pA + C1-pA) indicated proper hybridization by observing the blue color shift of the solution and formation of large aggregates, as well as the hybridized 4 nm Au A1 + C1 NPs, which are visually less intense (Figures S2A and S2C). Figures S2B and S2D show the normalized spectra of each functionalized NP as compared to the original unfunctionalized NP. The SPR peaks for the DNA-functionalized 13 nm Au NPs had shifted to 522 nm (A1), 523 nm (C1), 522 nm (A1-pA), and 522 nm (C1-pA), indicating proper bonding of the thiol-DNA to the surface (Figure S2B). As for the 4 nm Au NPs, the functionalized peaks shifted more dramatically to 519 nm (A1), 518 nm (C1), 517 nm (A1-pA), and 520 nm (C1-pA), as seen in Figure S2D. In addition to looking for the spectral

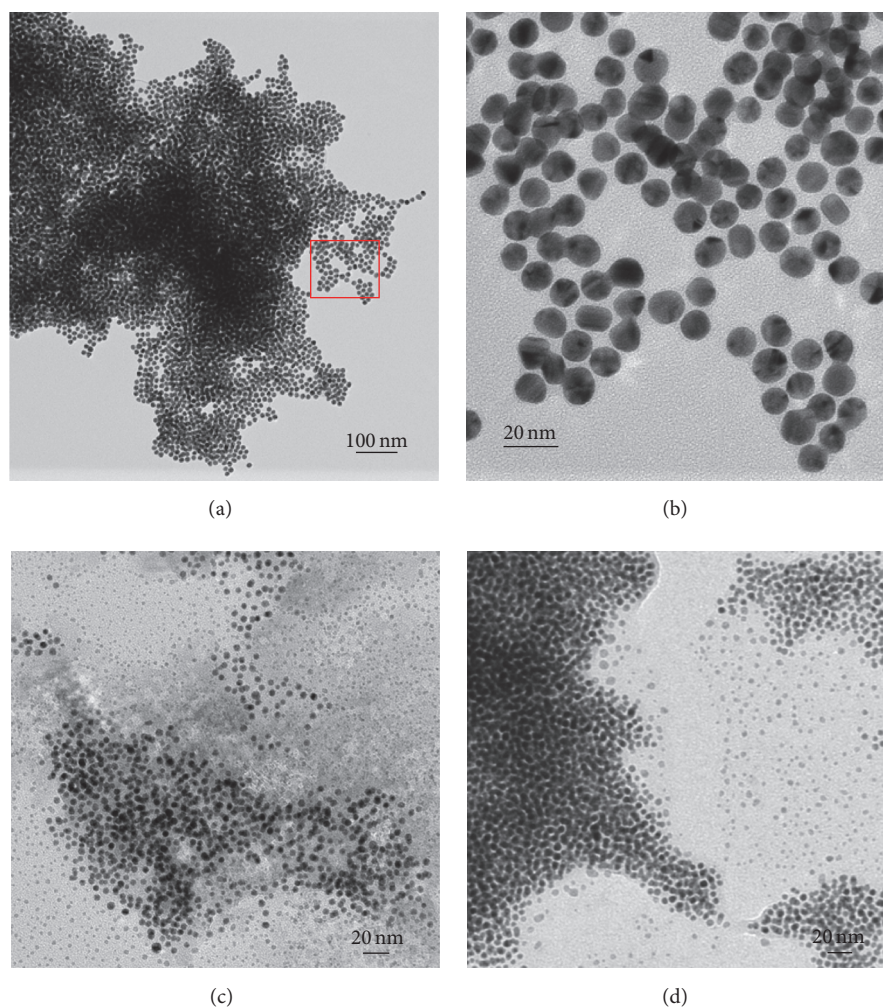


FIGURE 1: TEM imaging of functionalized and hybridized 13 nm Au NPs and hybridized 4 nm Au NPs. (a) Hybridized 13 nm Au A1 + C1 NPs. (b) Higher magnification TEM image of the boxed area in (a). (c) Hybridized 4 nm Au A1 + C1 NPs. (d) Hybridized 4 nm Au A1-pA + C1-pA NPs.

peak shifts, it was noted that an increased absorbance at the 280 nm wavelength was observed which indicates greater DNA presence on the sample.

To characterize the dehybridization temperature of the hybridized Au-DNA NPs, UV-Vis spectroscopy was performed on the sample by measuring the extinction at 280 nm while increasing the temperature of the sample. For the hybridized 13 nm Au-DNA NPs, the NPs were hybridized in a 100 mM NaCl and 25 mM Tris Acetate (pH 8.2) and the results are shown in Figure 2(a). The melting temperature (T_m) for the 13 nm Au A1 + C1 was $\sim 74^\circ\text{C}$ and for the 13 nm Au A1-pA + C1-pA NPs was $\sim 52^\circ\text{C}$, indicating that both hybridized complexes would stay intact after incubation with the cells at 37.0°C . Also, T_m 's for the 4 nm Au A1 + C1 NPs (300 mM NaCl) and the 4 nm Au A1-pA + C1-pA NPs (500 mM NaCl) are $\sim 79^\circ\text{C}$ and $\sim 71^\circ\text{C}$, respectively, indicating the complexes are robust enough for cell studies as well (Figure 2(b)). Visual inspection of the solutions after melt indicated that the NPs were in a dehybridized state due to the solution color shifting back to red.

3.3. Dynamic Light Scattering. DLS was used to verify an increase in NP diameter once the oligonucleotides were attached to the NPs and to observe agglomeration trends, with the results shown in Table 1. The measurements were only performed during the functionalization of the 13 nm Au NPs as verification of NP coverage and were not deemed necessary for the 4 nm Au NPs since other methods of verification were more adept for these particles. The unfunctionalized 13 nm Au NPs had an average hydrodynamic diameter of 15.3 nm, which increased to 39.7 nm and 33.9 nm once functionalized with the A1 and C1 sequences, respectively. The net surface charge became more negative when the ssDNA was immobilized on the surface of the Au NPs, as shown by the change from -9.67 mV for the citrate-stabilized 13 nm Au NPs to -45.9 mV and -47.1 mV for the NPs with the A1 and C1 sequences. However, the A1-pA and C1-pA functionalized NPs only increased to 21.1 nm and 27.7 nm in diameter, which shows the difference in the overall NP diameter when the poly-A sequence is present or not. Also, the shorter length of the ssDNA is reflected in its

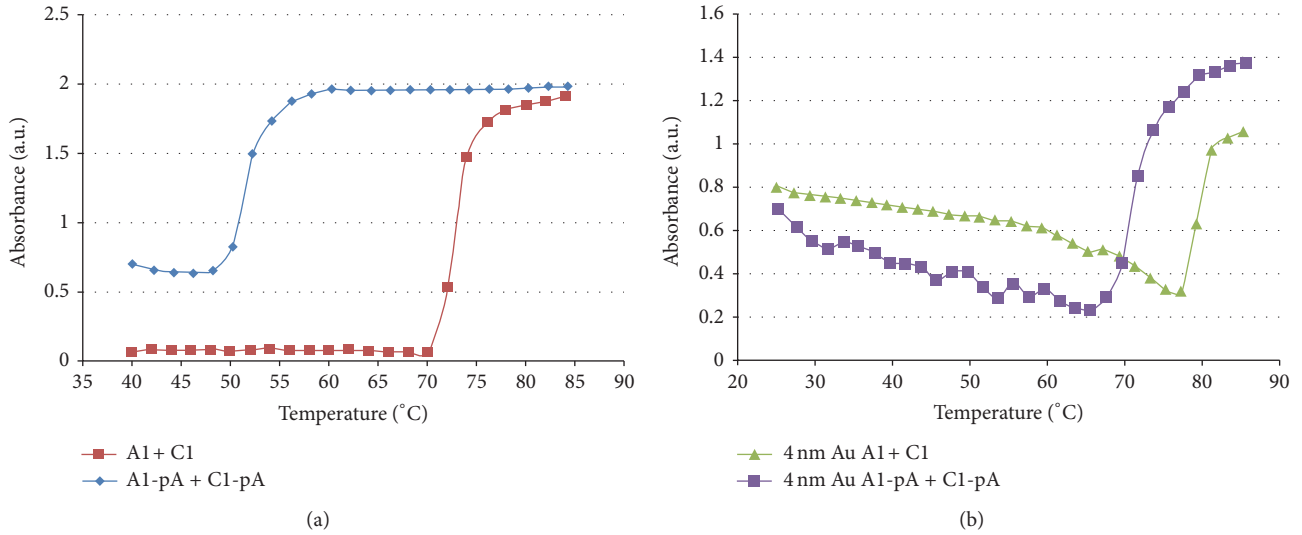


FIGURE 2: Dehybridization curves for hybridized 13 nm and 4 nm Au NPs. (a) Hybridized 13 nm Au NPs in 100 mM NaCl buffer. (b) Hybridized 4 nm Au NPs in 300 mM NaCl buffer (A1 + Cl) or 500 mM NaCl buffer (A1-pA + Cl-pA).

TABLE 1: Dynamic Light Scattering (DLS) and Laser Doppler Velocimetry (LDV) results for unfunctionalized and ssDNA functionalized 13 nm Au NPs.

Sample name	Z-ave (d-nm)	PdI	PdI width (d-nm)	ZP (mV)
<i>Particle only</i>				
13 nm Au	15.3	0.127	5.46	-9.67
<i>Functionalized particles</i>				
A1	39.7	0.211	18.2	-45.9
Cl	33.9	0.193	14.9	-47.1
A1-pA	21.1	0.126	7.47	-33.8
Cl-pA	27.7	0.231	13.3	-36.1

effect on surface charge of the NP, which only changed to -33.8 mV and -36.1 mV for the A1-pA and Cl-pA sequences due to the decreased number of phosphate groups. The two hybridized samples, A1 + Cl and A1-pA + Cl-pA, were not measured by DLS/LDV due to large aggregates forming and quickly precipitating from the solution which would not yield accurate results. It was noted that the A1 + Cl sample formed larger precipitates visually when compared to the A1-pA + Cl-pA sample (Figure S2A).

3.4. Hyperspectral Imaging. Hyperspectral imaging (HSI) was performed as a potential methodology for detecting NP binding state in a biological system in future studies since the LSPR of Au NPs can indicate the state of their immediate environment. The unfunctionalized 13 nm Au NPs had a spectrum with a main peak at ~ 650 nm and a shoulder occurring at ~ 590 nm (Figures 3(a) and 3(b)). The 13 nm Au A1 NPs exhibited two distinct spectra. The first peak occurring at ~ 525 nm is from the blue-green smaller particles in Figure 3(c), while the second peak at ~ 610 nm is from the red particles in the same image (Figures 3(c) and 3(d)). In Figure 3(e), the large network formed by the hybridized 13 nm Au A1 + Cl NPs can be easily seen, and the scattered

spectra from this sample had a peak between 650 nm and 670 nm, with the narrowest overall spectra of the 13 nm Au NP samples (Figure 3(f)). The 13 nm Au A1-pA + Cl-pA NPs also formed large networks with a similar spectrum to the A1 + Cl particles; however the peak was shifted slightly to the right with peaks occurring in the 670 nm to 680 nm range. The unfunctionalized and functionalized 4 nm Au NPs were too small to image using this system; however, a spectrum was collected from the hybridized 4 nm Au A1-pA + Cl-pA NPs, for comparison, with a primary peak between 580 nm and 610 nm and a very slight secondary peak around 650 nm (Figures 4(a) and 4(b)).

Next, it was evaluated whether the spectral signature obtained previously for the hybridized NPs could still be observed once the NPs were placed in a cellular environment and potentially internalized by the cell. In Figure 5(a), HaCaT control cells were scanned to provide a background spectrum to compare with the treated cells (Figure 5). Spectra obtained from the nonhybridized 13 nm Au A1-pA looked similar to the previously captured nonhybridized spectra with some additional spectra with peaks in the 550 nm range, which are likely from cellular structures when comparing the spectra to those obtained from the control cells (Figures 5(c) and

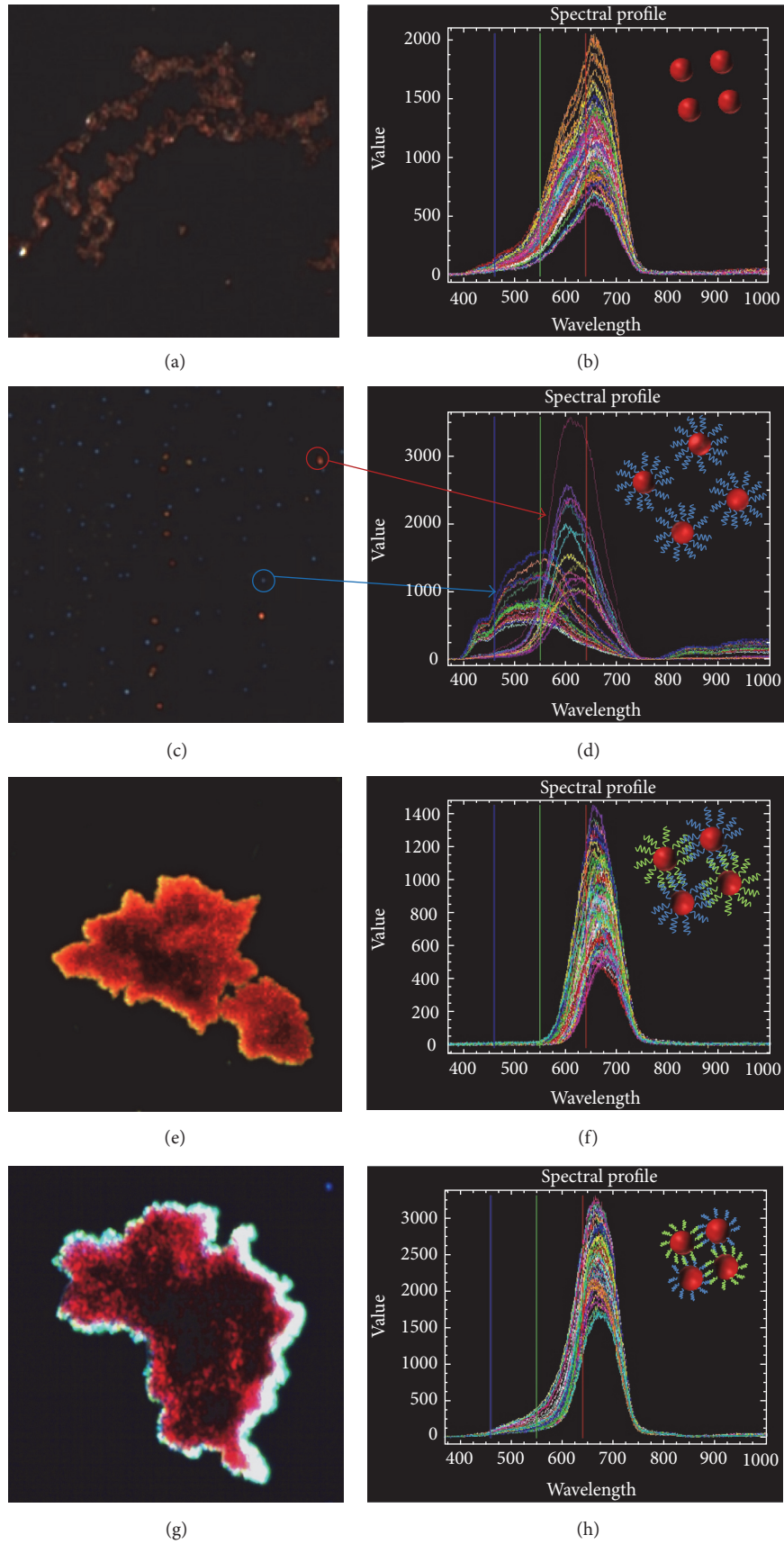


FIGURE 3: Hyperspectral imaging of unfunctionalized, functionalized, and hybridized 13 nm Au NPs. (a) Digital image and (b) spectra of unfunctionalized 13 nm Au NPs. (c) Digital image and (d) spectra of ssDNA functionalized 13 nm Au A1 NPs. (e) Digital image and (f) spectra of hybridized 13 nm Au A1 + C1 NPs. (g) Digital image and (h) spectra of hybridized 13 nm Au A1-pA + C1-pA NPs.

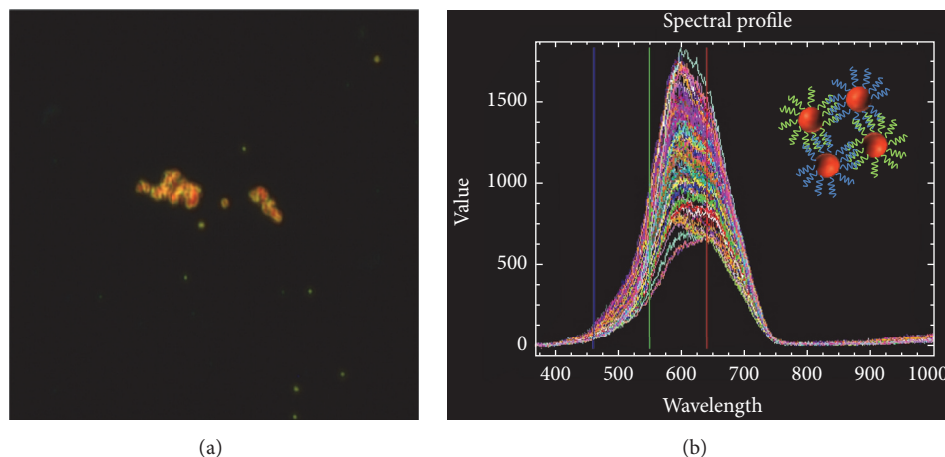


FIGURE 4: Hyperspectral imaging of hybridized 4 nm Au NPs. (a) Digital image and (b) spectra of hybridized 4 nm Au AI + CI NPs.

5(d)). The HaCaT cells treated with 13 nm Au AI + CI NPs were scanned and the Au-DNA aggregates can be seen localizing around the cells and potentially inside the cells (Figure 5(e)). Interestingly, the spectra collected appeared to be split between hybridized particles, group of peaks at ~ 655 nm, and nonhybridized particles, group at ~ 625 nm (Figure 5(f)). Similar results were seen with the 13 nm Au AI-pA + CI-pA NPs where the characteristic peak for these particles was observed at ~ 670 nm, with another group of spectra collected with bimodal distribution and peaks occurring at ~ 600 nm and ~ 660 nm (Figures 5(g) and 5(h)).

3.5. Biocompatibility. Cell viability (MTS) was assessed for the unfunctionalized, functionalized, and hybridized 13 nm Au NPs at 2.5 nM concentrations (Figure S3). For the 13 nm Au NPs, the only sample which displayed a significant impact on HaCaT cell viability was the 13 nm Au AI NP sample, which decreased viability slightly, to $\sim 81\%$ as compared to control cells (Figure S3).

3.6. Nanomaterial Uptake. To verify the uptake which appeared to be occurring microscopy imaging, TEM imaging was performed to confirm localization of NPs within the cells. HaCaT cells were treated with unfunctionalized 4 nm Au NPs and then prepared for TEM studies as previously described in Materials and Methods. Figures S4A and S4B show a large aggregate of NPs in the cytoplasm encased in a membrane-bound vacuole, possibly an endosome or lysosome. Upon further magnification, the NPs appear to be intact and have not significantly changed in morphology after 24 hours (Figure S4C). Also in Figure S4A, other smaller aggregates of NPs are present in the cytoplasm, and a much smaller group was observed to be located freely in the cytoplasm.

4. Conclusions

For the initial ssDNA functionalization work, 13 nm Au NPs were synthesized by the well-known Turkevich method with very high uniformity and reproducibility. Several techniques are available in the literature for the synthesis of 4-5 nm

Au NPs; however, they required the use of organic solvents with complicated ligand exchange processes for biofunctionalization. It was desired to have a biocompatible particle which would also be easy to functionalize, such as containing a citrate layer on the surface. In summary, it was found that extremely uniform and reproducible 4 nm Au NPs can be formed by using a sodium borohydride reduction of chloroauric acid in water at 4°C , followed by addition of sodium citrate which exchanges surface ions and helps to stabilize the solution. Regarding long term stability of the NPs, stock solutions have shown no change at 4 months after synthesis.

After synthesis of the NPs was completed, functionalization of the NMs was performed. DNA was chosen since it is relatively stable when combined with NMs and can be easily obtained in customizable sequences and double stranded DNA can be separated using thermal processes which could mimic a potential application of the particles in vitro. Characterization was performed to verify that the primary NPs were not changing during the functionalization process, the DNA was being successfully attached to the NPs, and the DNA was still functional through hybridization/dehybridization studies. The first set of sequences, AI and CI, are 25-mer sequences which contain a 10-mer poly-A sequence to move the binding part of the oligonucleotide away from the surface of the NP, and the second set, AI-pA and CI-pA, have the same 15-mer binding sequence without the poly-A spacer. This allowed observation of relative spacing of the hybridizing section from the surface of the NP and its effect on hybridization/dehybridization, which could be important for future applications. The effect of the poly-A sequence was evident on both NPs, where it was observed that the addition of the poly-A spacer increased the dehybridization temperature of the NPs, sometimes significantly, over the sequence without the poly-A spacer. This increase can be attributed to the greater freedom of movement and flexibility exhibited with the poly-A spacer present while steric hindrances may be more prevalent when the poly-A spacer is not present. The data appears to be pointing to the fact that this greater freedom of movement with the poly-A spacer would allow

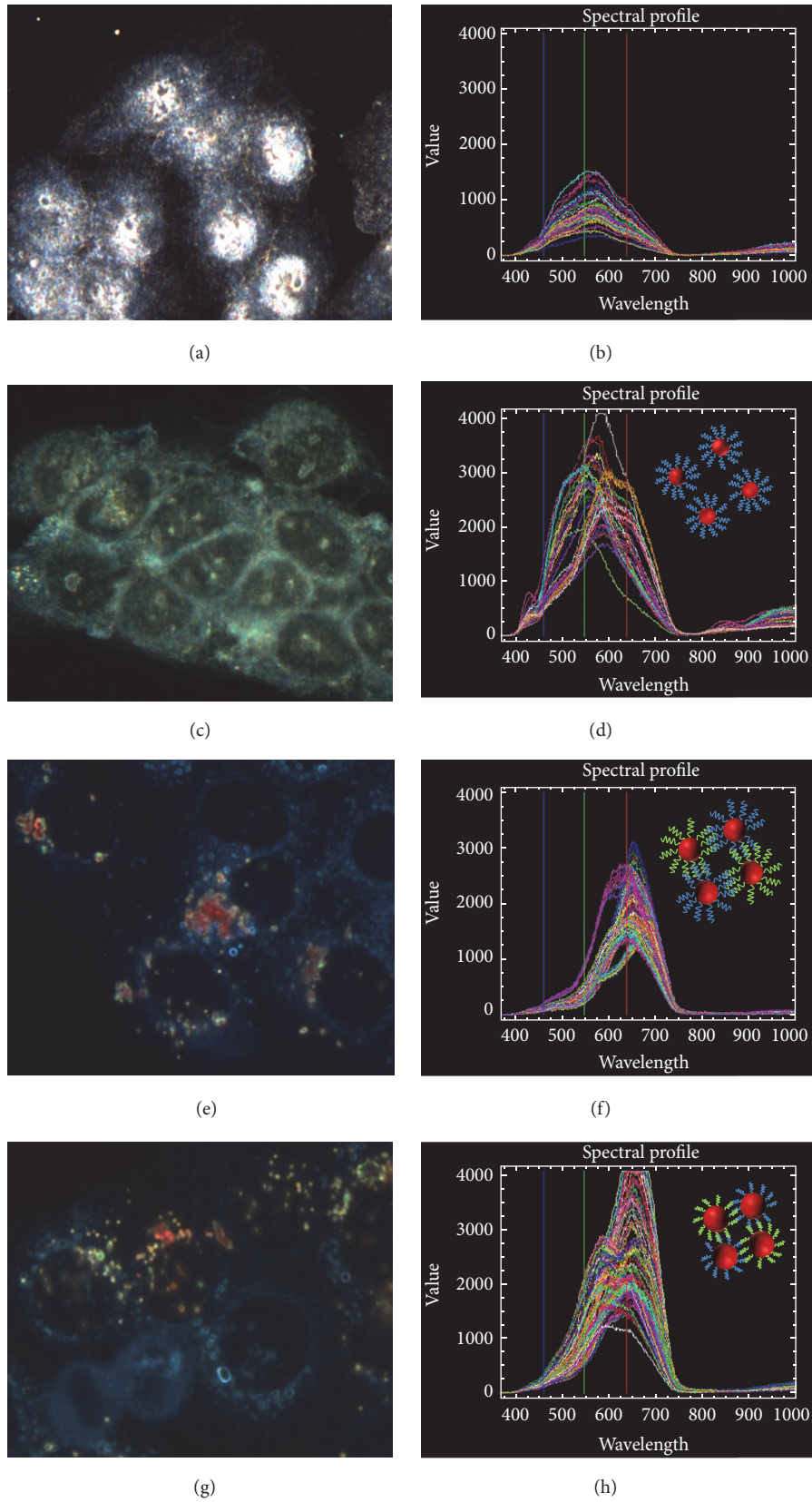


FIGURE 5: Hyperspectral imaging of untreated HaCaT cells and HaCaT cells treated with hybridized 13 nm Au NPs. (a) Digital image and (b) background spectra of untreated HaCaT cells. (c) Digital image and (d) spectra of HaCaT cells treated with 13 nm Au A1-pA NPs. (e) Digital image and (f) spectra of HaCaT cells treated with 13 nm Au A1 + Cl NPs. (g) Digital image and (h) spectra of HaCaT cells treated with 13 nm Au A1-pA + Cl-pA NPs.

the DNA to withstand greater NP movement at increased temperatures before being forced apart. Additionally, the increased thermodynamic stability of the NP conjugates with the poly-A spacer could allow for the conjugates to survive longer within the cellular environment. On an application note, the higher melting temperature could be a significant advantage for therapeutic applications where local heating of the NPs would controllably release NPs and/or their payload.

Biocompatibility assessment of oligonucleotide-coated 13 nm Au NPs was performed with the HaCaT cell line with only a slight decrease in viability seen with the functionalized 13 nm Au NPs (Figure S3). Uptake of large aggregates of the unfunctionalized 4 nm Au NPs was seen in HaCaT cells (Figure S4), indicating that uptake of large NP-DNA conjugates is possible and that the NPs could remain intact for at least 24 h. Also, since they would remain in conjugated form, this could provide a real-time method to track target binding with diminishing intensity and peak shift.

Finally, hyperspectral imaging was performed to evaluate changes in reflected spectral signatures of Au NPs once the particles are functionalized and hybridized. Also, it was examined if the unique spectral signatures are affected when inside a biological system. The technique was able to obtain scattering spectra from the unfunctionalized, functionalized, and hybridized 13 nm Au NPs and show unique differences between their spectra. The spectra obtained for the Au NPs, in Figure 5, in different states matched theoretical values, with some caveats. For 13 nm spherical Au NPs, Mie theory predicts peak scattering at 531 nm (water, 23°C) or 545 nm (silica – 1.52) when calculating using MiePlot. This does not correlate well with the 13 nm Au NPs prior to functionalization, most likely due to aggregation of the particles under the conditions necessary for HSI imaging, but does exhibit the red-shift of the scattered spectra under aggregation conditions (Figures 5(a) and 5(b)). After functionalization, the 13 nm Au NPs were more dispersed, as is apparent in Figure 5(c), and spectra from the individual particles in the field of view yielded peak scattering wavelengths that very closely match the Mie theory values, with only a few aggregates providing the red-shifted second peak in Figure 5(d). The hybridized particles in Figures 5(e), 5(f), 5(g), and 5(h) both displayed the expected red-shifted scattering peak of aggregated Au NPs; however, a slight red-shift in the peak scattering with the poly-A spacer removed due to closer interparticle distances and, more interestingly, the overall width of the scattering spectrum narrowed (Figure 5(h)). The hybridized 4 nm Au NPs produced a scattering peak that was slightly blue-shifted from the larger 13 nm Au NPs with the same DNA functionalization, which is due purely to the smaller particles constituting the aggregate. The HSI data showed promising results of real-time detection of the Au NP hybridization state while being localized near or inside the cells. The scattering peaks for the hybridized NPs appeared to be unchanged once placed in the cell environment and corresponded well with the previous spectra obtained. For example, the scattering peak for the functionalized, nonhybridized 13 nm Au NPs still produced a scattering peak at ~525 nm even within the cell environment (Figure 5(d)). However, the combined signal of the cell background and the hybridized NPs may

need to be separated using spectral unmixing techniques to help improve NP spectral identification. Also, multiple aggregates can be seen in many of the cells' cytoplasm, indicating uptake of the hybridized NPs, but this would need to be verified with ultramicrotome sectioning and will be addressed in future studies.

The future application is to be able to detect the binding state of NM-bound biomolecules (DNA, proteins, peptides, etc.) inside a biological environment. Au NPs provide feedback of changes in aggregation state through shifting of their SPR peak when in close proximity to a biomolecule or another particle, which is conventionally tracked using UV-Vis. However, UV-Vis is difficult to use with a biological system, especially if it is desired to leave the sample intact since lysing of the cells may be required with UV-Vis. Hyperspectral imaging allows for observation of the NPs in the cellular environment without disruption of the biological system. Noncellular applications of HSI tracking nanomaterial binding events may include nanomaterial-based sensors such as gold nanoparticle-aptamer colorimetric responses. HSI may offer advantages in this application over UV-Vis when the particles are in more complex environments or when the colorimetric response acts as an indicator of detection.

Although not presented in this manuscript, the HSI system can be adapted with a perfusion chamber and heated stage to keep the cells viable for an extended period of time while observing the NP scattering spectra. Using the ENVI software, the scattering spectra obtained for each of the nonhybridized Au-DNA NPs can be saved as a library resource so that once the functionalized and/or hybridized NPs were exposed to the cells, the software can identify the binding state of the NPs in the cellular environment. Future work in this area will involve examining scattering from hybridized particles of different shapes, such as rods or platelets, composite materials, or mixed material nanostructures to compare spectral differences.

Conflicts of Interest

The authors declare that there are no conflicts of interest regarding the publication of this paper.

Acknowledgments

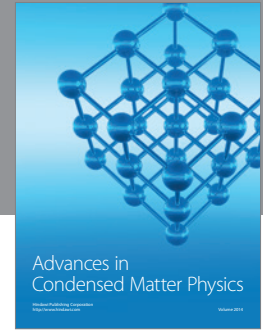
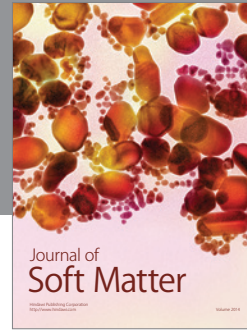
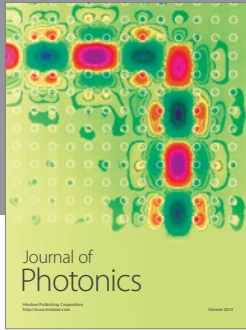
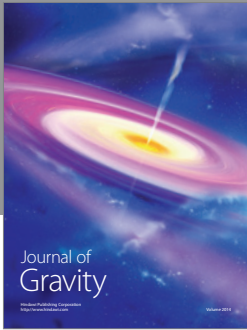
The authors would like to graciously thank Dr. Morley Stone for his continued support of this project. Additionally, the authors would like to recognize Col. Patricia Reilly, Dr. John J. Schlager, and Dr. Dan Powers for their support as well.

References

- [1] J. Chen, B. Wiley, Z.-Y. Li et al., "Gold nanocages: engineering their structure for biomedical applications," *Advanced Materials*, vol. 17, no. 18, pp. 2255–2261, 2005.
- [2] J. F. Hainfeld, D. N. Slatkin, and H. M. Smilowitz, "The use of gold nanoparticles to enhance radiotherapy in mice," *Physics in Medicine and Biology*, vol. 49, no. 18, pp. N309–N315, 2004.
- [3] L. R. Hirsch, R. J. Stafford, J. A. Bankson et al., "Nanoshell-mediated near-infrared thermal therapy of tumors under

- magnetic resonance guidance," *Proceedings of the National Academy of Sciences of the United States of America*, vol. 100, no. 23, pp. 13549–13554, 2003.
- [4] C. Loo, A. Lin, L. Hirsch et al., "Nanoshell-enabled photonics-based imaging and therapy of cancer," *Technology in Cancer Research and Treatment*, vol. 3, no. 1, pp. 33–40, 2004.
- [5] D. A. Giljohann, D. S. Seferos, W. L. Daniel, M. D. Massich, P. C. Patel, and C. A. Mirkin, "Gold nanoparticles for biology and medicine," *Angewandte Chemie—International Edition*, vol. 49, no. 19, pp. 3280–3294, 2010.
- [6] K. Saha, S. S. Agasti, C. Kim, X. Li, and V. M. Rotello, "Gold nanoparticles in chemical and biological sensing," *Chemical Reviews*, vol. 112, no. 5, pp. 2739–2779, 2012.
- [7] C. J. Murphy, A. M. Gole, S. E. Hunyadi et al., "Chemical sensing and imaging with metallic nanorods," *Chemical Communications*, vol. 8, no. 5, pp. 544–557, 2008.
- [8] R. Shukla, V. Bansal, M. Chaudhary, A. Basu, R. R. Bhonde, and M. Sastry, "Biocompatibility of gold nanoparticles and their endocytotic fate inside the cellular compartment: a microscopic overview," *Langmuir*, vol. 21, no. 23, pp. 10644–10654, 2005.
- [9] J. J. Li, L. Zou, D. Hartono, C. N. Ong, B. H. Bay, and L. Lanry Yung, "Gold nanoparticles induce oxidative damage in lung fibroblasts in vitro," *Advanced Materials*, vol. 20, no. 1, pp. 138–142, 2008.
- [10] Y. Pan, S. Neuss, A. Leifert et al., "Size-dependent cytotoxicity of gold nanoparticles," *Small*, vol. 3, no. 11, pp. 1941–1949, 2007.
- [11] X. Su and R. Kanjanawarut, "Control of metal nanoparticles aggregation and dispersion by PNA and PNA-DNA complexes, and its application for colorimetric DNA detection," *ACS Nano*, vol. 3, no. 9, pp. 2751–2759, 2009.
- [12] K.-W. Huang, C.-J. Yu, and W.-L. Tseng, "Sensitivity enhancement in the colorimetric detection of lead(II) ion using gallic acid-capped gold nanoparticles: Improving size distribution and minimizing interparticle repulsion," *Biosensors and Bioelectronics*, vol. 25, no. 5, pp. 984–989, 2010.
- [13] L. Li, B. Li, Y. Qi, and Y. Jin, "Label-free aptamer-based colorimetric detection of mercury ions in aqueous media using unmodified gold nanoparticles as colorimetric probe," *Analytical and Bioanalytical Chemistry*, vol. 393, no. 8, pp. 2051–2057, 2009.
- [14] A. Sugunan, C. Thanachayanont, J. Dutta, and J. G. Hilborn, "Heavy-metal ion sensors using chitosan-capped gold nanoparticles," *Science and Technology of Advanced Materials*, vol. 6, no. 3-4, pp. 335–340, 2005.
- [15] Z. Wang, J. H. Lee, and Y. Lu, "Label-free colorimetric detection of lead ions with a nanomolar detection limit and tunable dynamic range by using gold nanoparticles and DNazyme," *Advanced Materials*, vol. 20, no. 17, pp. 3263–3267, 2008.
- [16] S. Chah, M. R. Hammond, and R. N. Zare, "Gold nanoparticles as a colorimetric sensor for protein conformational changes," *Chemistry and Biology*, vol. 12, no. 3, pp. 323–328, 2005.
- [17] C. A. Mirkin, R. L. Letsinger, R. C. Mucic, and J. J. Storhoff, "A DNA-based method for rationally assembling nanoparticles into macroscopic materials," *Nature*, vol. 382, no. 6592, pp. 607–609, 1996.
- [18] J.-S. Lee, D. S. Seferos, D. A. Giljohann, and C. A. Mirkin, "Thermodynamically controlled separation of polyvalent 2-nm gold nanoparticle-oligonucleotide conjugates," *Journal of the American Chemical Society*, vol. 130, no. 16, pp. 5430–5431, 2008.
- [19] S. J. Hurst, H. D. Hill, and C. A. Mirkin, "Three-dimensional hybridization" with polyvalent DNA-gold nanoparticle conjugates," *Journal of the American Chemical Society*, vol. 130, no. 36, pp. 12192–12200, 2008.
- [20] D. S. Sebba and A. A. Lazarides, "Robust detection of plasmon coupling in core-satellite nanoassemblies linked by DNA," *Journal of Physical Chemistry C*, vol. 112, no. 47, pp. 18331–18339, 2008.
- [21] D. S. Sebba, T. H. LaBean, and A. A. Lazarides, "Plasmon coupling in binary metal core-satellite assemblies," *Applied Physics B*, vol. 93, no. 1, pp. 69–78, 2008.
- [22] M. R. Jones, R. J. MacFarlane, B. Lee et al., "DNA-nanoparticle superlattices formed from anisotropic building blocks," *Nature Materials*, vol. 9, no. 11, pp. 913–917, 2010.
- [23] N. M. Short, "Introduction: Technical and Historical Perspectives of Remote Sensing," <http://earthobservatory.nasa.gov/Features/RemoteSensing/>.
- [24] J. Turkevich, P. C. Stevenson, and J. Hillier, "The formation of colloidal gold," *Journal of Physical Chemistry*, vol. 57, no. 7, pp. 670–673, 1953.
- [25] G. Frens, "Controlled nucleation for the regulation of the particle size in monodisperse gold suspensions," *Nature Physical Science*, vol. 241, no. 105, pp. 20–22, 1973.
- [26] W. S. Sutherland and J. D. Winefordner, "Colloid filtration: a novel substrate preparation method for surface-enhanced Raman spectroscopy," *Journal of Colloid and Interface Science*, vol. 148, no. 1, pp. 129–141, 1992.
- [27] K. C. Grabar, R. G. Freeman, M. B. Hommer, and M. J. Natan, "Preparation and characterization of Au colloid monolayers," *Analytical Chemistry*, vol. 67, no. 4, pp. 735–743, 1995.
- [28] Z. Liang, J. Zhang, L. Wang, S. Song, C. Fan, and G. Li, "A centrifugation-based method for preparation of gold nanoparticles and its application in biodetection," *International Journal of Molecular Sciences*, vol. 8, no. 6, pp. 526–532, 2007.
- [29] R. G. DiScipio, "Preparation of colloidal gold particles of various sizes using sodium borohydride and sodium cyanoborohydride," *Analytical Biochemistry*, vol. 236, no. 1, pp. 168–170, 1996.
- [30] S. O. Obare, R. E. Hollowell, and C. J. Murphy, "Sensing strategy for lithium ion based on gold nanoparticles," *Langmuir*, vol. 18, no. 26, pp. 10407–10410, 2002.
- [31] R. T. Tom, V. Suryanarayanan, P. G. Reddy, S. Baskaran, and T. Pradeep, "Ciprofloxacin-protected gold nanoparticles," *Langmuir*, vol. 20, no. 5, pp. 1909–1914, 2004.
- [32] Y. Ding, X. Zhang, X. Liu, and R. Guo, "Studies on interactions of thionine with gold nanoparticles," *Colloids and Surfaces A: Physicochemical and Engineering Aspects*, vol. 290, no. 1–3, pp. 82–88, 2006.
- [33] R. C. Murdock, L. Braydich-Stolle, A. M. Schrand, J. J. Schlager, and S. M. Hussain, "Characterization of nanomaterial dispersion in solution prior to in vitro exposure using dynamic light scattering technique," *Toxicological Sciences*, vol. 101, no. 2, pp. 239–253, 2008.
- [34] W. Haiss, N. T. K. Thanh, J. Aveyard, and D. G. Fernig, "Determination of size and concentration of gold nanoparticles from UV-Vis spectra," *Analytical Chemistry*, vol. 79, no. 11, pp. 4215–4221, 2007.
- [35] P. C. Lee and D. Meisel, "Adsorption and surface-enhanced Raman of dyes on silver and gold sols," *Journal of Physical Chemistry*, vol. 86, no. 17, pp. 3391–3395, 1982.
- [36] P. Boukamp, R. T. Petrussevska, D. Breitkreutz, J. Hornung, A. Markham, and N. E. Fusenig, "Normal keratinization in a

- spontaneously immortalized aneuploid human keratinocyte cell line," *Journal of Cell Biology*, vol. 106, no. 3, pp. 761–771, 1988.
- [37] A. M. Schrand, J. J. Schlager, L. Dai, and S. M. Hussain, "Preparation of cells for assessing ultrastructural localization of nanoparticles with transmission electron microscopy," *Nature Protocols*, vol. 5, no. 4, pp. 744–757, 2010.
- [38] A. Curry, G. Nusz, A. Chilkoti, and A. Wax, "Substrate effect on refractive index dependence of plasmon resonance for individual silver nanoparticles observed using darkfield microspectroscopy," *Optics Express*, vol. 13, no. 7, pp. 2668–2677, 2005.
- [39] J. J. Mock, D. R. Smith, and S. Schultz, "Local refractive index dependence of plasmon resonance spectra from individual nanoparticles," *Nano Letters*, vol. 3, no. 4, pp. 485–491, 2003.
- [40] X. Liu, M. Atwater, J. Wang, and Q. Huo, "Extinction coefficient of gold nanoparticles with different sizes and different capping ligands," *Colloids and Surfaces B: Biointerfaces*, vol. 58, no. 1, pp. 3–7, 2007.



Hindawi

Submit your manuscripts at
<https://www.hindawi.com>

